Heliyon 6 (2020) e05548

Contents lists available at ScienceDirect

Heliyon

journal homepage: www.cell.com/heliyon

Research article

Influence of heating rate, temperature, pressure on the structure, and phase transition of amorphous Ni material: A molecular dynamics study

Hue Dang Thi Minh [a], Gelu Coman [b], Hoc Nguyen Quang [c], Dung Nguyen Trong [d,*]

[a] Faculty of Electrical and Electronics Engineering, Thuyloi University, 175 Tay Son, Dong Da, Hanoi, Viet Nam
[b] "Dunarea de Jos" University of Galati, Romania
[c] Faculty of Physics, Hanoi National University of Education, 136 Xuan Thuy, Cau Giay, Hanoi, Viet Nam
[d] Institute of Research and Development, Duy Tan University, Da Nang, 550000, Viet Nam

ARTICLE INFO

Keywords:
Materials science
Materials chemistry
Nanotechnology heating rate temperature pressure amorphous
Ni material structure phase transition
Molecular dynamics

ABSTRACT

The present article is aimed to investigate influence of the heating rate, temperature (T), pressure (P) on the structure and phase transition of amorphous Ni material with heating rate 2×10^5, 2×10^6 and 2×10^7 K/s at T = 300 K; T = 300, 400, 500, 600, 700, 800, 900 and 1000 K at heating rate 2×10^6 K/s; T = 300, 621 and 900 K at P = 1, 2, 3, 4 and 5 GPa by molecular dynamics simulation method with Sutton-Chen embedded potential and periodic boundary conditions. The structure of amorphous Ni material determined through the radial distribution function, the total energy, the size and the average coordination number. The phase transition and the glass transition temperature determined through the relationship between the total energy and temperature. The result shows that when the heating rate increases, the first peak's position for the radial distribution function is 2.45 Å and a constant, the first peak's height, the total energy and the size increase, the average coordination number decreases from 13 to 12. When temperature increases from 300 to 1000 K at P = 0 GPa, the position decreases from 2.45 Å to 2.40 Å, the average coordination number is 13 and a constant, glass transition temperature is 631 K, the total energy increases, the size increases and happens the phase transition from the amorphous state to the liquid state. When pressure increases from 0 GPa to 5 GPa at T = 300, 621 and 900 K, the position decreases, the height increases, the total energy increases, the size decreases, the average coordination number decreases from 13 to 12, that shows with amorphous Ni material when increasing heating rate, T, P lead to structural change, phase transition of materials is significant.

1. Introduction

Recently, amorphous nickel (Ni) material has significant application in the theoretical, experimental, and simulation research community. It is extensively used in different devices such as magnetic devices [1], biomedical microelectronics [2, 3, 4, 5, 6], magnetic resonance cameras [7], photocatalysts [8, 9], high speed storages [10], sensors [11], solar batteries [12, 13, 14, 15], sol-gel technologíe [16], microwaves [17], electrochemical equipments [18], intracellular precursors [19]. electrochemical reductions [20], nucleation techniques [21] and other fields of science and technology [22]. Besides, they also use amorphous Ni materials in many applications such as ceramic additives, capacitive materials, conductive pastes, coatings, lubricants, and electrodes [23, 24, 25]. To study and manufacture amorphous Ni materials, researchers use methods such as experimental methods, theory methods and simulation methods [26]. Experimental methods include the polyol synthesis [27], the chemical vapor deposition (CVD), the decomposition in liquid phase [28, 29, 30] and the gravimetric therapy (TG) [31]. Physical properties of amorphous Ni material depend on the structure, the shape and crystallization factors. These processes depend on synthetic, chemical and physical methods [32, 33, 34, 35]. Empirical methods used in the production process are very complex and it is difficult to control the shape and the size of amorphous Ni material [36]. Theoretical methods include the medium field theory [37], the Monte Carlo method (MC) [38], the contingent valuation method (CVM) [39], the Green function theory [40, 41], the effective mean-field theory [42] and the Bethe model [43]. Besides, there still are simulation methods and they are considered as one of the most superior research methods. By simulations, researchers can track the phase transition and change the physical properties from micro-level to macro-level. In simulating the structure, the phase

* Corresponding author.
E-mail address: dungntdt2018@gmail.com (D. Nguyen Trong).

https://doi.org/10.1016/j.heliyon.2020.e05548
Received 13 May 2020; Received in revised form 6 August 2020; Accepted 16 November 2020

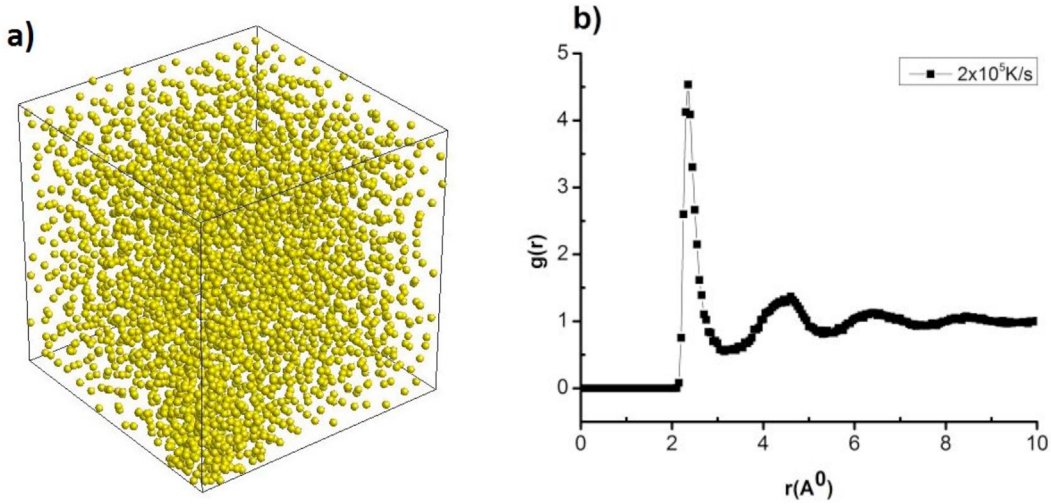

Figure 1. The structural features such as the shape (a), the radial distribution function (b) of amorphous Ni material with the heating rate of 2×10^5 K/s.

transition temperature and the crystallization process, the molecular dynamics (MD) method is a most popular tool for metal materials [44, 45, 46, 47, 48, 49, 50]. For experimental methods, materials sizes from 20 nm to 39.91 nm [51], the effect of heating rate and temperature on the shape (cube and sphere) are determined. In particular, the decrease in melting temperature depends on the size of Ni material. The structural characteristics of materials show that there is a direct correlation between the size and the area and the inverse ratio between the size and the volume [52] has led to a decline in melting curve [53] and has proven experimentally for many metals. This effect was studied by Pawlow [54] and shows experimentally by Takakagi [55]. The melting temperature of Au nanoparticles was determined using the MicroED method [56] and the size of nanoparticles did not observe [57]. Meanwhile, the phase transition of Ni material can be determined by stress or temperature of material [58, 59, 60, 61]. According to the empirical method of Ichikawa, the closest linking distance of Ni is 2.52 Å [62]. The melting temperature depends on the size of materials because the density of atoms at the surface layer is much larger than that in the material (the binding energy of atoms on the surface layer is smaller than that in the material). This phenomenon is determined successfully by Pawlow [54]. In addition, the structural characteristics of amorphous Ni material are determined as follows: the melting temperature is 1728 K [63], the Curie temperature is 631 K [64,65], the glass transition temperature is 630 K [66] and the crystallization temperature is 800 K [67]. In particular, appears the difference between the Curie temperature and the glass transition temperature of the material and that is caused the dependence of these quantities on the density, the bonding length and the radial distribution function [68, 69, 70, 71, 72]. By the empirical method Ichikawa shows that the closest linking distance is 2.43 Å [73] for bulk Ni, 2.45 Å [74] for Ni nanoparticles and 2.24 Å [75] for AlNi nanoparticles. Meanwhile, Ni material has the covalent radius of 1.21 Å [76], which shows that the Ni–Ni bond length is twice the covalent radius. Based on the obtained results on structural characteristics of Ni materials combined with our recent studies on the structure of nanomaterials such as Fe, Ni [66,77, 78], Ni [79], we continue to study the influence of temperature, pressure and depth of earth's surface on structural characteristic quantities of amorphous Ni materials by the MD method [80].

2. Method of calculation

To carry out the research process of amorphous Ni materials, we carry out some steps. In the first step, initially random sowing numbers atoms N = 3000 atoms Ni into the cube with the size ℓ and shown in the formula (1)

$$\rho = \frac{N}{V}, \ell = \left(\frac{N}{\rho}\right)^{1/3} \tag{1}$$

by the MD method with the embedded Sutton-Chen potential and periodic boundary conditions [81, 82, 83, 84]. This method is represented by Eq. (2)

$$E_{tot} = \sum_{i=1}^{N} \frac{1}{2} \sum_{j=1, j^1 i}^{N} \Phi(r_{ij}) + F(\rho_i), \Phi(r_{ij}) = \varepsilon \left(\frac{a}{r_{ij}}\right)^n, F(\rho_i) = -\varepsilon C \sum_{i=1}^{N} \sqrt{\rho_i}, \rho_i = \sum_{j=1, j^1 i}^{N} \rho(r_{ij}), \rho(r_{ij}) = \left(\frac{a}{r_{ij}}\right)^m \tag{2}$$

combined with the Verlet algorithm and the heating process by the laws of Nosé [85], Hoover [86]. In Eq. (2), E_{tot}, $\Phi(r_{ij})$, $F(\rho_i)$, ε, a, r_{ij}, ρ_i, C, N, n, m are constants, ε = 0.0073767 eV, a = 3.5157 Å, n = 10.0, m = 5.0, C = 84.745, r_c = 20 Å [87,88].

In the second step, materials run NVT recovery statistics (N, V, T = const) at T = 7000 K with 2×10^4 steps of MD simulation and the time for each MD step is 0.46 fs for the material to be stable in the liquid state. Then temperature decreases from 7000 K to 300 K and increases from 300 K to 400, 500, 600, 700, 800, 900 and 1000 K at P = 0 GPa. Similarly, pressure increases from zero to 1, 2, 3 and 4 GPa, at T = 300, 631 and 900 K. All materials run NVT, NVP with 2×10^4 steps of MD simulation and run NVE with 2×10^5 steps of MD simulation at corresponding temperatures and pressures.

In the third step, to determine the structure and the phase transition of amorphous Ni material, we determine the size ℓ, the total energy E_{tot}

Table 1. The structural characteristics of amorphous Ni material with different heating rates.

Heating speed (K/s)	2×10^5	2×10^6	2×10^7
r(Å)	2.45	2.45	2.45
g(r)	4.53	5.19	5.27
ℓ(nm)	3.28	3.23	3.23
E_{tot} (eV)	-13138	-13517	-13523
CN	13	13	13

Table 2. Structural characteristics of amorphous Ni material at different temperatures.

T(K)	300	400	500	600	700	800	900	1000
r(Å)	2.45	2.45	2.45	2.45	2.45	2.45	2.45	2.4
g(r)	5.19	4.78	4.30	4.23	3.98	3.93	3.53	3.36
ℓ(nm)	3.23	3.26	3.29	3.26	3.29	3.26	3.32	3.29
E_{tot}(eV)	-13517	-13448	-13350	-13295	-13245	-13202	-13143	-13105
CN	13	13	13	13	13	13	13	12

of the system and the radial distribution function (RDF) g(r) and shown in the formula (3)

$$g(r) = \frac{V}{N^2}\left\langle \frac{\Sigma_i n_i(r)}{4\pi r^2 \Delta r} \right\rangle \tag{3}$$

with the coordination number (CN) shown in the formula (4)

$$CN = 4\pi\rho \int_0^{r_1} g(r) r^2 dr \tag{4}$$

as determined in [89, 90]. Here, r is the first peak's position for the radial distribution function, g(r) is the first peak's height for the radial distribution function and the probability of finding an atom in the distance from r to r + Δr, $n_i(r)$ are the coordinates, V is the volume, N is the number of atoms and $\rho = 7.81$ g.cm^{-3} is the density.

In the fourth step 4, to check the accuracy of results, we use tools as the centrosymmetric parameter [91,92], the bond angle analysis [93], the bond order analysis [94] and the AFM analysis method to find the morphology of surface [95], fractal and multi-fractal geometric structures determined directly from the database [96].

3. Results and discussion

3.1. Effect of heating rate

With different heating rates, structural characteristics of amorphous Ni material are shown in Figure 1 and Table 1.

At the heating rate of 2×10^5 K/s, then amorphous Ni material has a cubic shape shown in yellow color (Figure 1a) with the dimension ℓ = 3.28 nm, the total energy E_{tot} = -13138 eV, the average coordinate number CN = 13, and the first peak's position of the RDF $r_{Ni\text{-}Ni}$ = 2.45 Å, the first peak's height of the RDF g(r) = 4.53 (Figure 1b). With the Sutton-Chen dip interaction, our obtained Ni–Ni binding length is $r_{Ni\text{-}Ni}$ = 2.45 Å and this result is in good agreement with previously published results $r_{Ni\text{-}Ni}$ = 2.43 Å [73], $r_{Ni\text{-}Ni}$ = 2.45 Å [74], $r_{Ni\text{-}Ni}$ = 2.24 Å [66] and is twice than the covalent radius 1.21 Å [76]. When the heating speed increases from 2×10^5 K/s to 2×10^6 and 2×10^7 K/s, the coordination number CN is 13 and constant, the position $r_{Ni\text{-}Ni}$ is 2.45 Å and constant, the height g(r) increases from 4.53 to 5.27, the size ℓ decreases from 3.28 nm to 3.23 nm. The total energy E_{tot} decreases from -13138 eV to -13517 and -13523 eV and the size increases dramatically at the heating rate of 2×10^7 K/s. That leads to an increase in the size of amorphous Ni material because the density of atoms decreases. The size of amorphous Ni material is broken at the heating rate of 2×10^7 K/s (Table 2). These results are useful for future experimental studies.

3.2. Effect of temperature

Next, studying the effect of temperature (T) on structural characteristics and the obtained results are shown in Figure 2.

The amorphous Ni material at T = 300 K has a cube shape, the size is ℓ = 3.23 nm, the total energy E_{tot} = -13517 eV, the density of atoms is evenly distributed and is represented by dark blue (Figure 2a), the position is $r_{Ni\text{-}Ni}$ = 2.45 Å and the height g(r) = 5.19. When temperature

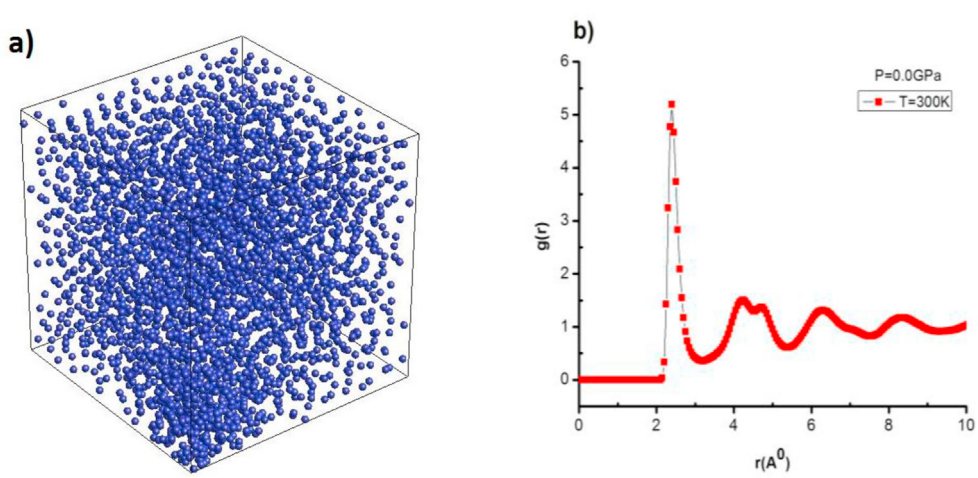

Figure 2. The shape (a) and the radial distribution function (b) of amorphous Ni material at T = 300 K.

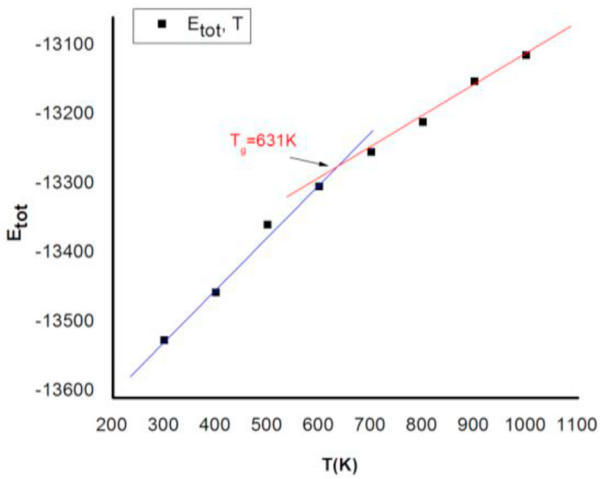

Figure 3. Phase transition of amorphous Ni material at different temperatures.

increases from 300 to 400, 500, 600, 700, 900 and 1000 K, the shape of the Ni material changes, the size ℓ increases from 3.23 nm to 3.29 nm, the total energy E_{tot} increases from -13517 to -13448, -13350, -13295, -13245, -13202, -13143 and -13105 eV, the position is $r_{Ni\text{-}Ni} = 2.45$ Å and constant, the height g(r) decreases from 5.19 to 4.78, 4.30, 4.23, 3.98, 3.93, 3.53 and 3.36 (Table 2). When temperature increases, the total energy of the system increases. The relationship between temperature and the total energy is shown in Figure 3. When temperature increases from 300 to 400, 500, 600, 700, 800, 900 and 1000 K, the total energy increases from -13517 to -13448, -13350, - 13295, -13245, -13202, -13143 and -13105 eV. In the range from 300 to 600 K, the total energy increases slowly and is shown in blue lines. When temperature increases and is larger than 700 K, the total energy increases faster and is shown in the red line. The intersection of the blue line and the red line at the point T = 631 K is called as the glass phase transition point or glass temperature T_g, This result is in very good agreement with experiments and simulations [64, 65, 66], calculations and stress changes of Ni in NiAl alloys [97,98].

3.3. Effect of pressure

Pressure is increased from 1 GPa to 2, 3 and 4 GPa at T = 300, 631 and 900 K and the simulated results are shown below.

3.3.1. At temperature T = 300 K

Structural characteristics and the phase transition of amorphous Ni material at T = 300 K and different pressures are shown in Figure 4.

The amorphous Ni material at T = 300 K and P = 0 GPa has the cube shape (Figure 4a), the first peak's position of the RDF is $r_{Ni\text{-}Ni} = 2.45$ Å, the first peak's height of the RDF g(r) = 5.19 (Figure 4b), the size $\ell = 3.23$ nm, the total energy E_{tot} = -13517 eV and the CN = 13. When pressure increases from zero to 1, 2, 3 and 4 GPa, the shape of the material changes, the first peak's position decreases from 2.45 Å to 2.20, 2.10, 2.05 and 2.05 Å; the first peak's height g(r) changes from 5.19 to 6.05, 6.11, 6.22 and 6.04 (Figure 4c); the size ℓ decreases from 3.23 nm to 2.89, 2.78, 2.71 and 2.66 nm (Figure 4d); the total energy E_{tot} increases from -13517 eV to -10624, -6935, -3081 and 625 eV (Figure 4e); the CN decreases from 13 to 12 (Figure 4f) te when pressure increases, the density of atoms decreases.

3.3.2. At temperature T = 631 K

Structural characteristics and the phase transition of amorphous Ni material at T = 631 K and different pressures are shown in Figure 5.

The amorphous Ni material at T = 631 K and P = 0 GPa has the cube shape (Figure 5a), the first peak's position of the RDF is $r_{Ni\text{-}Ni} = 2.45$ Å, the first peak's height of the RDF g(r) = 4.23 (Figure 5b), the size $\ell = 3.26$ nm, the total energy E_{tot} = -13295 eV and the CN = 13. When pressure increases from zero to 1, 2, 3 and 4 GPa, the shape of the material changes, the first peak's position decreases from 2.45 Å to 2.20, 2.10, 2.05 and 2.05 Å; the first peak's height g(r) changes from 4.23 to 5.67,

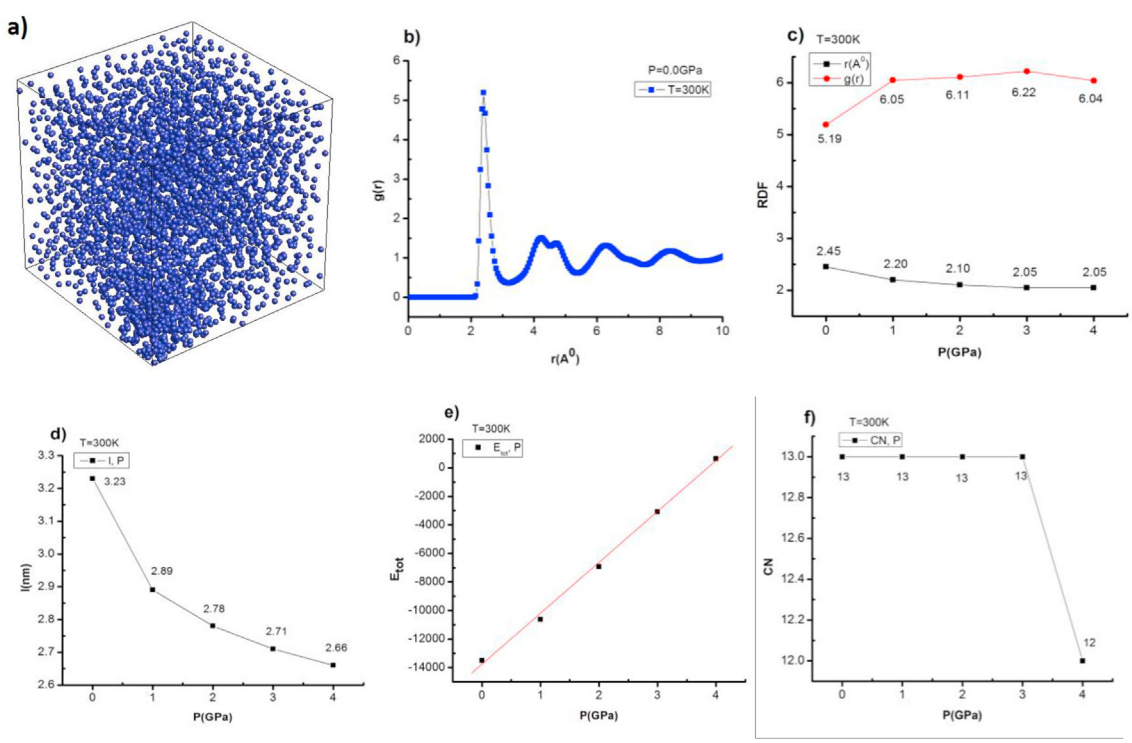

Figure 4. The shape (a), the RDF (b) at P = 0 GPa; the RDF (c), the size (d), the total energy (e) and the CN (f) for amorphous Ni material at T = 300 K and different pressures.

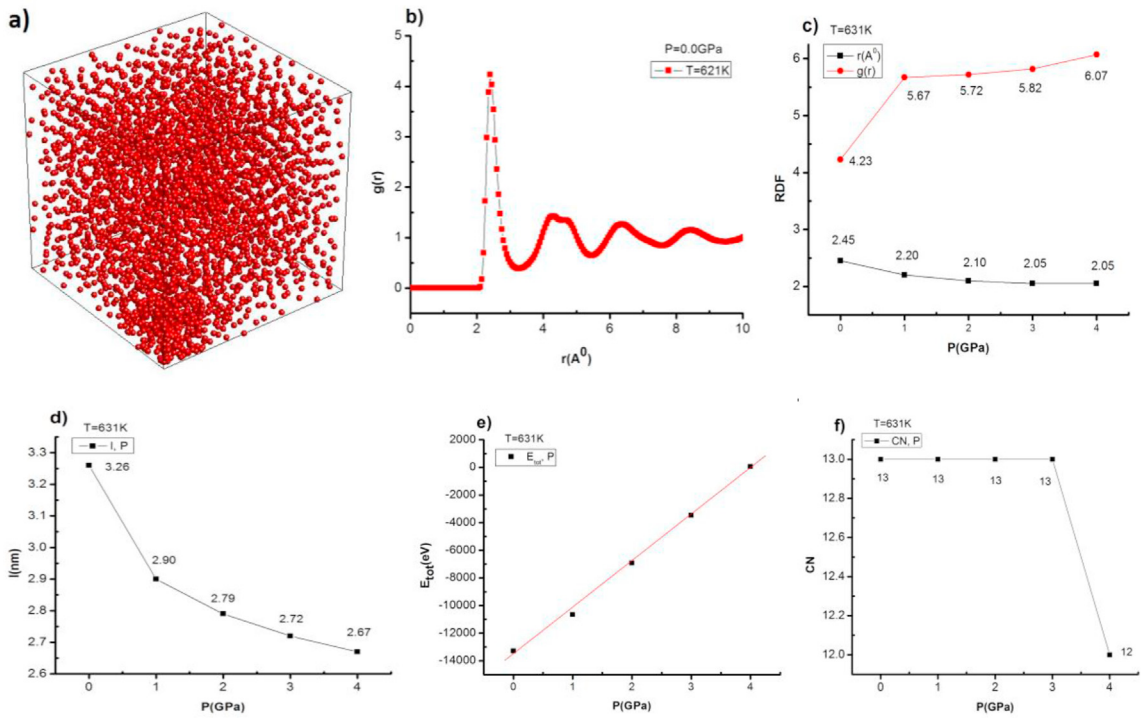

Figure 5. The shape (a), the RDF (b) at P = 0 GPa; the RDF (c), the size (d), the total energy (e) and the CN (f) for amorphous Ni material at T = 631 K and different pressures.

5.72, 5.82 and 6.07 (Figure 5c); the size ℓ decreases from 3.26 nm to 2.90, 2.79, 2.72 and 2.67 nm (Figure 5d); the total energy E_{tot} increases from -13295 eV to -10655, -6918, -3469 and 52 eV (Figure 5e); the CN decreases from 13 to 12 (Figure 5f) te when pressure increases, the density of atoms decreases.

3.3.3. At temperature T = 900 K

Structural characteristics and the phase transition of amorphous Ni material at T = 900 K and different pressures are shown in Figure 6.

The amorphous Ni material at T = 900 K and P = 0 GPa has the cube shape (Figure 6a), the first peak's position of the RDF is $r_{Ni\text{-}Ni}$ = 2.45 Å, the first peak's height of the RDF g(r) = 3.53 (Figure 6b), the

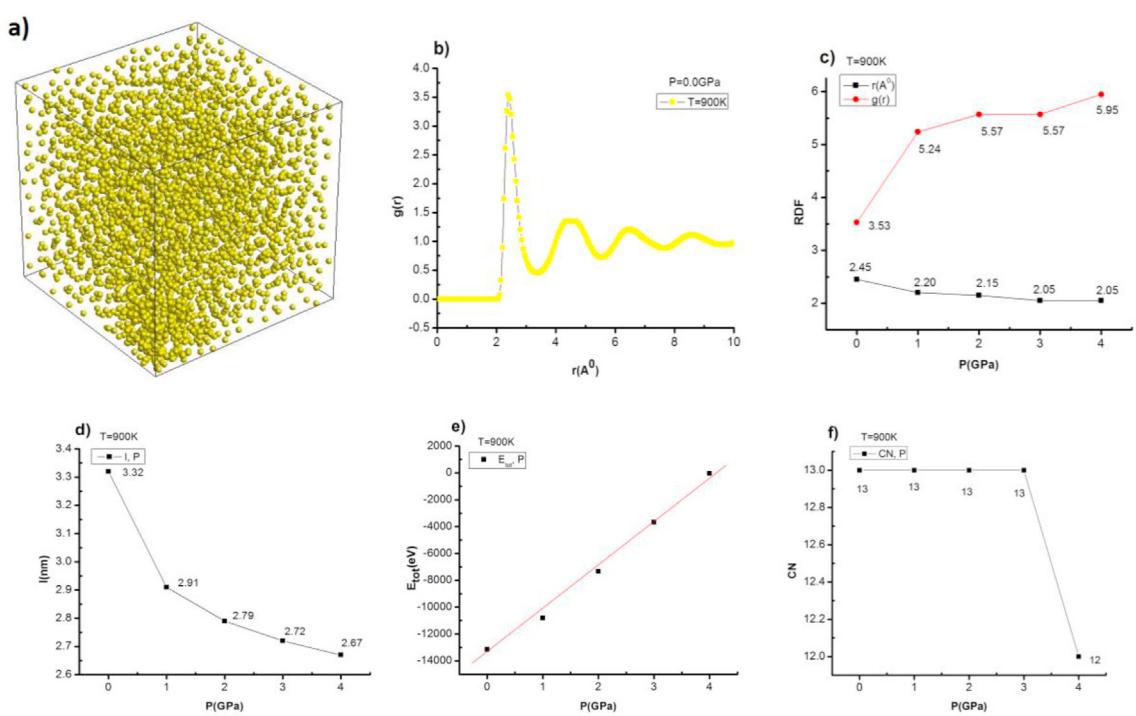

Figure 6. The shape (a), the RDF (b) at P = 0 GPa; the RDF (c), the size (d), the total energy (e) and the CN (f) for amorphous Ni material at T = 900 K and different pressures.

size ℓ = 3.32 nm, the total energy E_{tot} = -13143 eV and the CN = 13. When pressure increases from zero to 1, 2, 3 and 4 GPa, the shape of the material changes, the first peak's position decreases from 2.45 Å to 2.20, 2.15, 2.05 and 2.05 Å; the first peak's height g(r) changes from 3.53 to 5.24,5.57,5.57 and 5.95 (Figure 6c); the size ℓ decreases from 3.32 nm to 2.91, 2.79, 2.72 and 2.67 nm (Figure 6d); the total energy E_{tot} increases from -13143 eV to -10800, -7327, -3675 and -32 eV (Figure 6e); the CN decreases from 13 to 12 (Figure 6f) te when pressure increases, the density of atoms decreases. For amorphous Ni material when the heating rate increases, the first peak's position of the RDF is $r_{Ni\text{-}Ni}$ = 2.45 Å and constant. When temperature increases from 300 K to 1000 K at P = 0 GPa and when pressure increases from zero to 1, 2, 3 and 4 GPa at T = 300, 631 and 900 K, the first peak's position of the RDF $r_{Ni\text{-}Ni}$ decreases. For amorphous Ni material, the structure only changes when temperature T > 900 K and pressure P > 0 GPa. The obtained results are very useful basis for the future experiments such as determining the change in structure and phase transition of amorphous Ni material.

4. Conclusion

We studied the effect of the heating rate, temperature and pressure on structural characteristics of amorphous Ni material by the MD method with the Sutton-Chen embedded potential and periodic boundary conditions. The resulting material is nano-sized and shown in dark blue. When the heating rate increases from 2×10^5 K/s to 2×10^6 and 2×10^7 K/s, the size of amorphous Ni material increases, the total energy of the system increases and increases dramatically at the heating rate of 2×10^7 K/s. When temperature increases from 300 K to 400, 500, 600, 700, 800, 900 and 1000 K, the size and the total energy increase. In particular, when temperature increases from 300 K to 600 K, then the total energy increases slowly. When temperature increases from 600 K to 1000 K, the total energy increases rapidly and the glass phase transition happens at T_g = 631 K. When pressure increases at T = 900 K, the size decreases faster than at T = 300 K and 621 K. When pressure increases in a liquid state, the size decreases more than in an amorphous state. When temperature increases from 300 K to 1000 K, the first peak's position of the RDF decreases from 2.45 Å to 2.40 Å, the first peak's height of the RDF decreases from 5.19 to 3.36 and the average coordination number decreases from 13 to 12. When pressure increases at T = 300, 631 and 900 K, the first peak's position of the RDF decreases from 2.45 Å to 2.05 Å. When pressure increases at T = 900 K, the first peak's height of the RDF greatly increases. When pressure increases, the density of atoms at a liquid state increases faster than that in an amorphous state and the CN decreases from 13 to 12. Therefore, the Ni material always exists in an amorphous state. When temperature increases, the material changes from an amorphous state to a liquid state at T = 1000 K and when pressure increasé, the amorphous Ni material has largest change of the first peak's height for the RDF at T = 900 K. The obtained results will serve as a basis for future experimental research.

Declarations

Author contribution statement

Hue Dang Thi Minh, Dung Nguyen Trong: Conceived and designed the experiments; Performed the experiments; Analyzed and interpreted the data; Contributed reagents, materials, analysis tools or data; Wrote the paper.

Gelu Coman, Hoc Nguyen Quang,: Analyzed and interpreted the data; Contributed reagents, materials, analysis tools or data; Wrote the paper.

Data availability statement

Data included in article/supp. material/referenced in article.

Funding statement

This research did not receive any specific grant from funding agencies in the public, commercial, or not-for-profit sectors.

Declaration of interests statement

The authors declare no conflict of interest.

Additional information

No additional information is available for this paper.

References

[1] S. Ingole, P. Manandhar, J.A. Wright, E. Nazaretski, J.D. Thompson, S.T. Picraux, Assembly and magnetic properties of nickel nanoparticles on silicon nanowires, Appl. Phys. Lett. 94 (1-3) (2009) 223118.
[2] G. Busca, Chapter 9 - metal catalysts for hydrogenations and dehydrogenations, in: Heterogeneous Catalytic Materials, Elsevier, Amsterdam, 2014, pp. 297–343.
[3] M.A. Lucchini, A. Testino, C. Ludwig, A. Kambolis, M. El-Kazzi, A. Cervellino, P. Riani, F. Canepa, Continuous synthesis of nickel nanopowders: characterization, process optimization, and catalytic properties, Appl. Catal. B Environ. 156 – 157 (2014) 404–415.
[4] N.J. Rajput, Methods of preparation of nanoparticles - a review, Int. J. Adv. Eng. Technol. 7 (11) (2015) 1806.
[5] E.G.C. Neiva, M.M. Oliveira, L.H. Marcolino, A.J.G. Zarbin, Nickel nanoparticles with hcp structure: preparation, deposition as thin films and application as electrochemical sensor, J. Colloid Interface Sci. 468 (2016) 34–41.
[6] Y. Zhao, Y. Wang, F. Ran, Y. Cui, C. Liu, Q. Zhao, Y. Gao, D. Wang, S. Wang, A comparison between sphere and rod nano particles regarding their in viv obiol ogical be havior and pharmaco-kinetics, Sci. Rep. 7 (1) (2017) 4131.
[7] J. Kim, S. Park, J.E. Lee, S.M. Jin, J.H. Lee, I.S. Lee, I. Yang, J.S. Kim, S.K. Kim, M.H. Cho, T. Hyeon, Designed fabrication of multifunctional magnetic gold nanoshells and their application to magnetic resonance imaging and photothermal therapy, Angew. Chem. Int. Ed. 45 (2006) 7754–7758.
[8] M. Usman, W.M.A. Wan Daud, H.F. Abbas, Dry reform-ing of methane: influence of process parameters - a review, Renew. Sustain. Energy Rev. 45 (2015) 710–744.
[9] T. Cinar, T. Gurkaynak Altincekic, Synthesis and investiga-tion of bimetallic Ni-Co/Al2O3 nanocatalysts using the polyol pro-cess, Part. Sci. Technol. 34 (6) (2016) 725–735.
[10] S.D. Bader, Colloquium: opportunities in nanomagnetism, Rev. Mod. Phys. 78 (2006) 1.
[11] N. Sattarahmady, H. Heli, R.D. Vais, An electrochemical acetylcholine sensor based on lichen-like nickel oxide nanostructure, Biosens. Bioelectron. 48 (2013) 197–202.
[12] Y. Ruan, C. Wang, J. Jiang, Nanostructured Ni compounds as electrode materials towards high-performance electrochemical capacitors, J. Mater. Chem. 38 (4) (2016) 14509–14538.
[13] L. Gaouyat, Z. He, J.-F. Colomer, D. Schryvers, F. Mirabella, O. Deparis, in: Linking Optical Properties and Nanostructure of NiCrOx Cermet Nanocomposite for Solar Thermal Application, Springer Netherlands, Dordrecht, 2015, 497-497.
[14] Andreas Jossen, Juergen Garche, Dirk Uwe Sauer, Operation conditions of batteries in PV applications, Sol. Energy 76 (6) (2004) 759–769.
[15] M. Glavin, W.G. Hurley, Battery management system for solar energy applications, IEEE Pers. Account (2006) 79–83, 9486625.
[16] J. Yang, B. Feng, Y. Liu, Y. Zhang, L. Yang, Y. Wanga, M. Wei, J. Lang, D. Wang, X. Liu, Phase transition and magnetic properties of Mg-doped hexagonal close-packed Ni nanoparticles, Appl. Surf. Sci. 254 (2008) 7155–7158.
[17] C. Parada, E. Morán, Microwave-assisted synthesis and magnetic study of nanosized Ni/NiO materials, E. Chem. Mater 18 (2006) 2719–2725.
[18] E.O. Zayim, I. Turhan, F.Z. Tepehan, N. Ozer, Sol–gel deposited nickel oxide films for electrochromic applications, Solar E. Mater. Sol. Cell. 92 (2008) 164–169.
[19] Y. Chen, X. Luo, G.H. Yue, X. Luo, D.L. Peng, Synthesis of iron–nickel nanoparticles via a nonaqueous organometallic route, Mater. Chem. Phys. 113 (2009) 412–416.
[20] Y.T. Jeon, J.Y. Moon, G.H. Lee, J. Park, Y. Chang, Comparison of the magnetic properties of metastable hexagonal close-packed Ni nanoparticles with those of the stable face-centered cubic Ni nanoparticles, J. Phys. Chem. B 110 (2006) 1187–1191.
[21] M. Grzelczak, J. Perez-Juste, B. Rodriguez-Gonzalez, M. Spasova, I. Barsukov, M. Farle, L.M. Liz-Marzan, Pt-catalyzed growth of Ni nanoparticles in aqueous CTAB solution, Chem. Mater. 20 (2008) 5399–5405.
[22] S.P. Gubin, Y.A. Koksharov, G.B. Khomutov, G.Y. Yurkov, Magnetic nanoparticles: preparation, structure and properties, Russ. Chem. Rev. 74 (6) (2005) 489–520.
[23] Chunhua Feng, Zhisheng Lv, Xiaoshuang Yang, Chaohai Wei, Anode modification with capacitive materials for a microbial fuel cell: an increase in transient power or stationary power, Phys. Chem. Chem. Phys. 16 (2014) 10464–10472.
[24] T. Yonezawa, Nickel alloys: properties and characteristics, Compr. Nucl. Mater. 2 (2012) 233–266.
[25] A. Azor, M.L. Ruiz-Gonzalez, F. Gonell, C. Laberty-Robert, M. Parras, C. Sanchez, D. Portehault, J.M. Gonz alez-Calbet, Nickel-doped sodium cobaltite 2D nanomaterials: synthesis and electrocata-lytic properties, Chem. Mater. 30 (15) (2018) 4986–4994.

[26] H. Kachkachi, Effects of spin non-collinearities in magnetic nanoparticles, J. Magn. Magn Mater. 316 (2) (2007) 248–254.
[27] E.G.C. Neiva, M.F. Bergamini, M.M. Oliveira, L.H. Marcolino Jr., A.J.G. Zarbin, PVP-capped nickel nanoparticles: synthesis, characterization and utilization as a glycerol electro sensor, Sensor. Actuator. B 196 (2014) 574–581.
[28] P. Samyn, A. Barhoum, T. €Ohlund, A. Dufresne, Review: nanoparticles and nanostructured materials in papermaking, J. Mater. Sci. 53 (1) (2018) 146–184.
[29] B.M. Abu-Zied, A.M. Asiri, An investigation of the ther-mal decomposition of nickel citrate as a precursor for NiNiO com-posite nanoparticles, Thermochim. Acta 649 (2017) 54–62.
[30] L.A. Kafshgari, M. Ghorbani, A. Azizi, Synthesis and char-acterization of manganese ferrite nanostructure by co-precipitation, sol-gel, and hydrothermal methods, Part. Sci. Technol. 36 (2018) 1–7.
[31] Ghanbarabadi Hassan, Behnam Khoshandam, Thermogravimetric synthesis of Ni nanoparticles with varied morphologies and particle sizes, Part. Sci. Technol. (2019) 1–9.
[32] H. Schmidt, Nanoparticles by chemical synthesis, processing to materials and innovative applications, Appl. Organomet. Chem. 15 (2001) 331–343.
[33] K.-C. Huang, S.H. Ehrman, Synthesis of iron nanoparticles via chemical reduction with palladium ion seeds, Langmuir 23 (2007) 1419–1426.
[34] D.V. Goia, Preparation and formation mechanisms of uniform metallic particles in homogeneous solutions, J. Mater. Chem. 14 (2004) 451–458.
[35] H. Forster, C. Wolfrum, W. Peukert, Experimental study of metal nanoparticle synthesis by an arc evaporation/condensation process, J. Nanoparticle Res. 14 (2012) 926.
[36] Y.-T. Foo, J.E.-M. Chan, G.-C. Ngoh, A.Z. Abdullah, B.A. Horri, B. Salamatinia, Synthesis and characterization of NiO and Ni nanoparticles using nanocrystalline cellulose (NCC) as a tem-plate, Ceram. Int. 43 (18) (2017) 16331–16339.
[37] F. Michael, C. Gonzalez, V. Mujica, M. Marquez, M.A. Ratner, Size dependence of ferromagnetism in gold nanoparticles: mean field results, Phys. Rev. B 76 (22) (2007) 224409.
[38] L. Jiang, J. Zhang, Z. Chen, Q. Feng, Z. Huang, Monte Carlo study of magnetic properties for the mixed spin-3/2 and spin-1 ferrimagnetic nanoparticles, Phys. B Condens. Matter 405 (1) (2010) 420–424.
[39] H. Wang, Y. Zhou, D. Lin, C. Wang, Phase diagram of ising nano-particles with cubic structures, Phys. Status Solidi 232 (2) (2002) 254–263.
[40] A. Zaim, M. Kerouad, Monte Carlo simulation of the compensation and critical behaviors of a ferrimagnetic core/shell nanoparticle ising model, Phys. Stat. Mech. Appl. 389 (17) (2010) 3435–3442.
[41] Y. Yuksel, E. Aydıner, H. Polat, Thermal and magnetic properties of a ferrimagnetic nanoparticle with spin-3/2 core and spin-1 shell structure, J. Magn. Magn Mater. 323 (23) (2011) 3168–3175.
[42] W. Jiang, H. yu Guan, Z. Wang, A. bang Guo, Nanoparticle with a ferrimagnetic interlayer coupling in the presence of single-ion anisotropis, Phys. B Condens. Matter 407 (3) (2012) 378–383.
[43] B. Deviren, M. Keskin, Y. Aydin, Compensation temperatures, magnetic susceptibilities and phase diagrams of a mixed ferrimagnetic ternary system on the 101 bethe lattice, JETP Lett. 92 (4) (2010) 214–222.
[44] J. Lu, J.A. Szpunar, Applications of the embedded-atom method to glass formation and crystallization of liquid and glass transition-metal nickel, Philos. Mag. A 75 (1997) 1057–1066.
[45] Y. Qi, T. Çagin, W.L. Johnson, W.A. Goddard III, Melting and crystallization in Ni nanoclusters: the mesoscale regime, J. Chem. Phys. 115 (2001) 385–394.
[46] Y.-H. Wen, Z.-Z. Zhu, R. Zhu, G.-F. Shao, Size effects on the melting of nickel nanowires: a molecular dynamics study, Phys. E 25 (2004) 47–54.
[47] Y. Zhang, L. Wang, W. Wang, Thermodynamic, dynamic and structural relaxation in supercooled liquid and glassy Ni below the critical temperature, J. Phys. Condens. Matter 19 (2007) 196106.
[48] P.H. Kien, Study of structural and phase transition of nickel metal, ISRN Mater. Sci. 2 (2014) 1–6, 253627.
[49] A.N. Andriotis, Z.G. Fthenakis, M. Menon, Correlated variation of melting and Curie temperatures of nickel clusters, Phys. Rev. B Condens. Matter 75 (2007), 073413.
[50] H.M. Lu, P.Y. Li, Z.H. Cao, X.K. Meng, Size-, shape-, and dimensionality-dependent melting temperatures of nanocrystals, J. Phys. Chem. C 113 (2009) 7598–7602.
[51] Toshitaka Ishizaki, Kenichi Yatsugi, Kunio Akedo, Effect of particle size on the magnetic properties of Ni nanoparticles synthesized with trioctylphosphine as the capping agent, Nanomaterials (Basel) 6 (9) (2016) 172.
[52] D.K. Pattadar, F.P. Zamborini, Size stability study of catalytically active sub-2 nm diameter gold nanoparticles synthesized with weak stabilizers, J. Am. Chem. Soc. 140 (2018) 14126–14133.
[53] W. Luo, W. Hu, S. Xiao, Size effect on the thermodynamic properties of silver nanoparticles, J. Phys. Chem. C 112 (2008) 2359–2369.
[54] P. Pawlow, Ober die Abhängigkeit des Schmelzpunktes von der Oberflächenenergie eines festen Körpers (Zusatz.), Z. Phys. Chem. 65 (1909) 545–548.
[55] M. Takagi, Electron-Diffraction study of liquid-solid transition of thin metal films, J. Phys. Soc. Jpn. 9 (1954) 359–363.
[56] S.L. Lai, J.Y. Guo, V. Petrova, G. Ramanath, L.H. Allen, Size-dependent melting properties of small tin particles: nanocalorimetric measurements, Phys. Rev. Lett. 77 (1996) 99–102.
[57] M. Zhang, E.A. Olson, R.D. Twesten, J.G. Wen, L.H. Allen, I.M. Robertson, I. Petrov, In situ transmission electron microscopy studies enabled by microelectromechanical system technology, J. Mater. Res. 20 (2005) 1802–1807.
[58] Valery I. Levitas, Arunabha M. Roy, Dean L. Preston, Multiple twinning and variant-variant transformations in martensite: phase-field approach, Phys. Rev. B 88 (2013), 054113.
[59] Valery I. Levitas, Arunabha M. Roy, Multiphase phase field theory for temperature- and stress-induced phase transformations, Phys. Rev. B 91 (2015) 174109.
[60] I. Valery, M.Roy Levitas Arunabha, Multiphase phase field theory for temperature-induced phase transformations: formulation and application to interfacial phases, Acta Mater. 109 (2016).
[61] M. Arunabha, Roy, Effects of interfacial stress in phase field approach for martensitic phase transformation in NiAl shape memory alloys, Appl. Phys. A 126 (2020) 576.
[62] T. Ichikawa, S. Ogawa, Electron diffraction study of the local atomic arrangement in thin films of amorphous gallium, iron and nickel, J. Phys. Colloq. 35 (27-29) (1974) C4.
[63] W. Martienssen, H. Warlimont, Springer Handbook Ofcondensed Matter and Materials Data, Springer, Berlin, 2005.
[64] X. He, H. Shi, Size and shape effects on magnetic properties of Amorphous Ni nanoparticles, Particuology 10 (4) (2012) 497–502.
[65] C.Q. Sun, W.H. Zhong, S. Li, B.K. Tay, H.L. Bai, E.Y. Jiang, Coordination imperfection suppressed phase stability of ferromagnetic, ferroelectric, and superconductive nanosolids, J. Phys. Chem. 108 (3) (2004) 1080–1084, 235B.
[66] Tuan Tran-Quoc, Dung Nguyen-Trong, Study of the factors affecting the heterogeneous kinetics of amorphous Ni nanoparticles using the simulation method, Int. J. Appl. Chem. 16 (1) (2020) 35–51.
[67] Trong Dung Nguyen, Chinh Cuong Nguyen, Vinh Hung Tran, Molecular dynamics study of microscopic structures, phase transitions and dynamic crystallization in Ni nanoparticles, RSC Adv. 7 (2017) 25406–25413.
[68] J. Daniel, Lacks, First-order amorphous-amorphous transformation in silica, Phys. Rev. Lett. 84 (2000) 4529–4532.
[69] G. Guitierrez, B. Johansson, Molecular dynamics study of structural properties of amorphous Al2O3, Phys. Rev. B 65 (2002) 104202–104210.
[70] Vo Van Hoang, Suhk Kun Oh, Annealing effects on structure in amorphous A12O3 models, Physica B 364 (2005) 225–232.
[71] Vo Van Hoang, Glass of monatomic Lennard-Jones system at nanoscale, Phys. B Condens. Matter 405 (2010) 1908–1914.
[72] Vo Van Hoang, T. Odagaki, M. Engel, Cooling rate effects on structure and thermodynamics of amorphous nanoparticles, Appl. Surf. Sci. 254 (2008) 7531–7534.
[73] T. Ichikawa, Electron diffraction study of the local atomic arrangement in amorphous Iron and Nickel films, Phys. Status Solidi 19 (2) (1973) 707–716.
[74] P.H. Kien, M.T. Lan, N.T. Dung, P.K. Hung, Annealing study of amorphous bulk and nanoparticle iron using molecular dynamics simulation, Int. J. Mod. Phys. B 28 (23) (2014) 17, 1450155.
[75] Dung Nguyen-Trong, Phuong Nguyen-Tri, Factors affecting the structure, phase transition and crystallization process of AlNi nanoparticles, J. Alloys Compd. 812 (2020) 152133.
[76] Atomic Radii of the Elements, Data Page, Wikipedia, 2016.
[77] L. Néel, Théorie du trainage magnétique des ferromagnétiques en grains fins avec applications aux Terres Cuites, Ann. Geophys. 5 (1949) 99–136.
[78] W.-Z. Han, L. Huang, S. Ogata, H. Kimizuka, Z.-C. Yang, C. Weinberger, Q.-J. Li, B.-Y. Liu, X.-X. Zhang, J. Li, E. Ma, Z.-W. Shan, From "smaller is stronger" to "size-independent strength plateau": towards measuring the ideal strength of iron, Adv. Mater 27 (2015) 3385.
[79] Sulekh Chandra, Avdhesh Kumar Praveen, Kumar Tomar, Synthesis of Ni nanoparticles and their characterizations, J. Saudi Chem. Soc. 18 (5) (2014) 437–442.
[80] H. Tsuzuki, P.S. Branicio, J.P. Rino, Structural characterization of deformed crystals by analysis of common atomic neighborhood, Comput. Phys. Commun. 177 (2007) 518–523.
[81] A.P. Sutton, J. Chen, Long-range finnis–sinclair potentials, Phil. Mag. Lett. 61 (1990) 139–146.
[82] M.S. Daw, M.I. Baskes, Semiempirical, quantum mechanical calculation of hydrogen embrittlement in metals, Phys. Rev. Lett. 50 (1983) 1285–1288.
[83] M.S. Daw, M.I. Baskes, Embedded-atom method: derivation and application to impurities, surfaces, and other defects in metals, Phys. Rev. B 29 (1984) 6443–6453.
[84] R. Yamamoto, T. Mihara, K. Taira, M. Doyama, Amorphous structures of iron obtained by quenching of the liquid state, Phys. Lett. 70 (1) (1979) 41–43.
[85] S. Nos´e, A unified formulation of the constant temperature molecular dynamics methods, J. Chem. Phys. 81 (1984) 511–519.
[86] W.G. Hoover, Canonical dynamics: equilibrium phase-space distributions, Phys. Rev. 31 (1985) 1695–1697.
[87] T. Çag̃, Nanoengineered Nanofibrous Materials, in: Y. Qi, H. Li, Y. Kimura, H. Ikeda, W.L. Johnson, W.A. Goddard III (Eds.), MRS Symp. Ser. 554, 1999, pp. 43–48.
[88] Y. Kimura, Y. Qi, T. Çag in, W.A. Goddard III, Technical Report , Pasadena: Caltech ASCI 3, 1998, pp. 1–29.
[89] P.K. Hung, D.K. Belashchenko, V.M. Chieu, N.T. Duong, V.V. Hoang, T.B. Van, Local structure of amorphous canonical systems, J. Metastable Nanocryst. Mater. 2 (6) (1999) 393–398.
[90] P.K. Hung, P.N. Nguyen, T.V. Mung, On the estimation of hydrogen diffusion parameters in amorphous and crystalline irons, J. Non-Cryst. Solids 356 (2010) 1262–1266.
[91] C.L. Kelchner, S.J. Plimpton, J.C. Hamilton, Dislocation nucleation and defect structure during surface indentation, Phys. Rev. B 58 (1998) 11085–11088.
[92] J. Li Modell, AtomEye: an efficient atomistic configuration viewer, Simul. Mater. Sci. Eng. 11 (2003) 173.
[93] G.J. Ackland, A.P. Jones, Applications of local crystal structure measures in experiment and simulation, Phys. Rev. B Condens. Matter 73 (2006), 054104.

[94] P.J. Steinhardt, D.R. Nelson, M. Ronchetti, Bond-orientational order in liquids and glasses, Phys. Rev. B 28 (1983) 784–805.
[95] Ş. Ţălu, M. Bramowicz, S. Kulesza, V. Dalouji, S. Solaymani, S. Valedbagi, Fractal features of carbon–nickel composite thin flms, Microsc. Res. Tech. 79 (2016a) 1208–1213.
[96] Ş. Ţălu, M. Bramowicz, S. Kulesza, V. Dalouji, M. Ilkhani, A. Ghaderi, S. Solaymani, Influence of annealing process on surface micromorphology of carbon–nickel composite thin flms, Opt. Quant. Electron. 49 (2017) 204.
[97] A.M. Roy, Influence of interfacial stress on microstructural evolution in NiAl alloys, Jetp Lett. (2020) 1–7.
[98] Sami H. Mahmood, Computational Methods in Material Science-Editorial, Mat. Sci. Res. I.; Special Issue 17 (2020) 1–2.